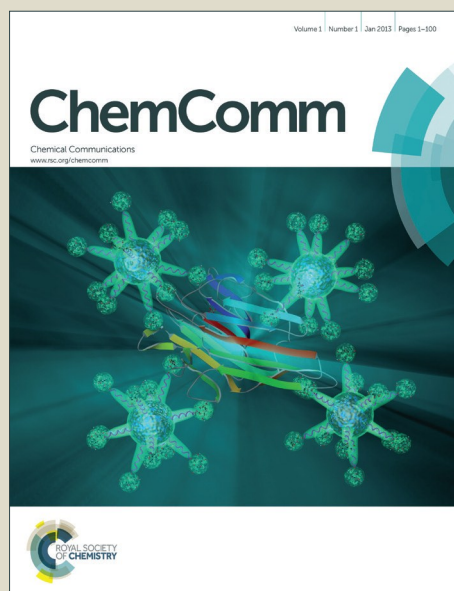


ChemComm

Accepted Manuscript



This is an *Accepted Manuscript*, which has been through the Royal Society of Chemistry peer review process and has been accepted for publication.

Accepted Manuscripts are published online shortly after acceptance, before technical editing, formatting and proof reading. Using this free service, authors can make their results available to the community, in citable form, before we publish the edited article. We will replace this *Accepted Manuscript* with the edited and formatted *Advance Article* as soon as it is available.

You can find more information about *Accepted Manuscripts* in the [Information for Authors](#).

Please note that technical editing may introduce minor changes to the text and/or graphics, which may alter content. The journal's standard [Terms & Conditions](#) and the [Ethical guidelines](#) still apply. In no event shall the Royal Society of Chemistry be held responsible for any errors or omissions in this *Accepted Manuscript* or any consequences arising from the use of any information it contains.



Journal Name

COMMUNICATION

Core-shell nanoparticles by silica coating of metal oxides in a dual-stage hydrothermal flow reactor

H. L. Hellstern^a, A. Mamakhel^a, M. Bremholm^a, B. B. Iversen^aReceived 00th January 20xx,
Accepted 00th January 20xx

DOI: 10.1039/x0xx00000x

www.rsc.org/

γ -Fe₂O₃@SiO₂, TiO₂@SiO₂, and α -Fe₂O₃@SiO₂ core-shell nanoparticles were synthesized by a surfactant-free hydrothermal method in a continuous flow dual-stage reactor. Uniform silica shells of 2 nm thickness were obtained when grown on γ -Fe₂O₃ and TiO₂ nanoparticles while thicker and more irregular shells were deposited on α -Fe₂O₃ due to low pH.

Core-shell nanoparticles are an important class of materials. A secondary material can be deposited on the core for multiple purposes incl. functionalization, protection from oxidation or agglomeration and improvement of catalytic performance.^{1,2} Silica is a frequently used shell material for coating of core nanoparticles including TiO₂,³⁻⁶ Au,^{7,8} Fe₂O₃,^{9,10} Fe₃O₄,¹¹⁻¹⁴ ZnO,^{15,16} and it can be used to improve dispersibility of the core nanoparticle.¹⁷ SiO₂ can be synthesized from tetraethyl orthosilicate (TEOS) through hydrolysis and condensation in a typical sol-gel process.¹⁸ Typical shell thicknesses are in the range of 20-100 nm, but silica shell thickness as low as 4 nm has been demonstrated.⁶ Functionalization of the silica surface with organic molecules allows the coated nanoparticle to be used as a biosensor or in medicine.¹⁹

Hydrothermal flow reactors are powerful tools for continuous synthesis of nanoparticles with narrow size distributions.²⁰ However, traditional single-stage flow reactors are typically not suited for synthesis of hybrid nanoparticles as nucleation and growth of the core and the shell occur simultaneously under identical reaction conditions which can lead to solid solutions or simple mixtures of single-phase nanoparticles.

In batch experiments synthesis of core-shell nanoparticles is usually a two-step process in which the primary core particle is synthesized prior to the secondary material used for the shell. For some

syntheses the shell material may nucleate at a higher temperature than the core which makes a one-pot synthesis possible, but this severely restraints the nanocomposites available for synthesis and doping effects have to be considered.

Here we report surfactant-free syntheses of γ -Fe₂O₃@SiO₂, TiO₂@SiO₂ and α -Fe₂O₃@SiO₂ core-shell nanoparticles in a dual-stage hydrothermal flow reactor, which separates the synthesis of core and shell into separate regions but maintains continuous production.²¹ Hydrothermal flow synthesis of the core material in the primary reactor stage produces nanoparticles of a narrow size distribution.²² Deposition of the shell material in the secondary reactor allows for thin nanoshells due to the short residence time. Shell thicknesses for γ -Fe₂O₃@SiO₂ and TiO₂@SiO₂ nanocomposites were approximately 2 nm, while the α -Fe₂O₃@SiO₂ shell thickness was up to 5 nm and more irregular. The formation of thin, complete shells or thick, incomplete shells is linked to the final pH and the isoelectric point of the core nanoparticles synthesized in the primary reactor.

All syntheses were performed in a hydrothermal continuous flow dual-stage reactor. The details of the dual-stage flow reactor has been described elsewhere,²¹ and an outline of the setup is illustrated in Supporting Information (Figure S1). 0.1 M ammonium iron(III) citrate (AIC) (Reactant #1) was pumped at 5 mL/min and mixed with degassed demineralized water at 15 mL/min heated to 350 °C in a tee mixer and led into the primary reactor for γ -Fe₂O₃ formation. The nanoparticle suspension was cooled down and then mixed with 0.2 M TEOS (Reactant #2) in isopropanol pumped at 5 mL/min, and the mixture was heated in the secondary reactor (100 °C). The composite product was cooled down and collected from a proportional relief valve. Anatase TiO₂ nanoparticles were synthesized in the primary reactor at 350 °C from 0.05 M titanium tetraisopropoxide (TTIP, 97%) in isopropanol mixed with heated solvent. Solvent was a 1 mM solution of acetic acid to adjust the pH to approximately 4. The TTIP precursor was pumped into the system at 5 mL/min, and the solvent was pumped at 12 mL/min. The cold suspension was mixed with 0.2

^a Center for Materials Crystallography, Department of Chemistry and iNANO, Aarhus University, Langelandsgade 140, 8000, Aarhus C, Denmark. Corresponding author: bo@chem.au.dk

Electronic Supplementary Information (ESI) available: [details of any supplementary information available should be included here]. See DOI: 10.1039/x0xx00000x

M TEOS in isopropanol pumped at 5 mL/min, and the mixture was heated in the secondary reactor (100°C). The volume of each reactor section is approximately 20 mL, and residence times were roughly 60 seconds for each reactor stage. For α -Fe₂O₃@SiO₂ the iron precursor was 0.1 M Fe(NO₃)₃(aq). Single-phase α -Fe₂O₃ nanoparticles were synthesized in a separate experiment using only the primary reactor stage at 250°C, 300°C, 350°C and 400°C. All of the above mentioned chemicals were purchased from Sigma-Aldrich.

Powder X-ray Diffraction (PXRD) data was collected in Bragg-Brentano geometry (Rigaku SmartLab, Cu K α ₁) and Rietveld refinements were performed using the FullProf²³ software. Structural models from the ICSD database (γ -Fe₂O₃ ICSD 247036, TiO₂ anatase ICSD-92363 and α -Fe₂O₃ ICSD-5840) were used for the initial models. Data was refined on a linearly interpolated background. Instrumental broadening was accounted for by using a LaB₆ standard. Peak profile was the Thompson-Cox-Hastings function. All diffraction patterns were refined by the Rietveld method and parameters are summarized in Supporting Information, Table S1.

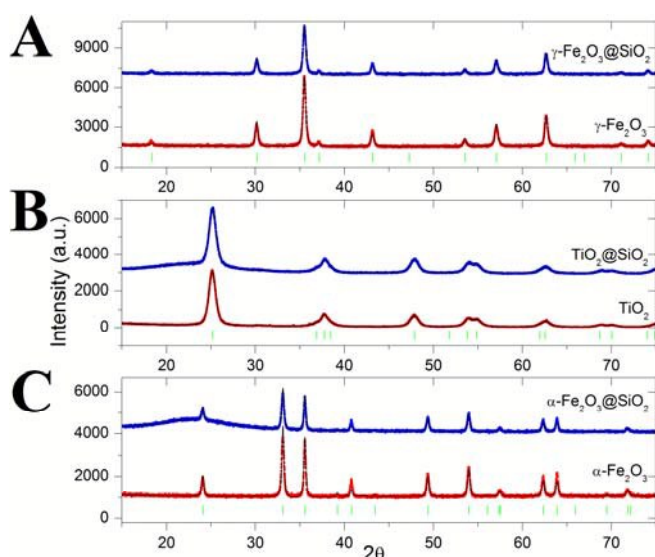


Figure 1: PXRD data for A) γ -Fe₂O₃@SiO₂ and γ -Fe₂O₃. B) TiO₂@SiO₂ and TiO₂. C) α -Fe₂O₃@SiO₂ and α -Fe₂O₃. Bragg reflections (green tick marks) and model intensities from Rietveld refinements (solid back lines) are included for each pattern. Blue lines (top) are nanocomposites while red lines (bottom) are the phase pure metal oxide. A broad feature from amorphous silica can be seen at around 25°.

Samples were investigated with Scanning Transmission Electron Microscopy (STEM) (FEI Talos F220A, operated at 200 kV) including Transmission Electron Microscopy (TEM), High Angle Annular Dark Field (HAADF) and Energy Dispersive X-ray spectroscopy (EDX). Elemental composition was investigated with X-Ray Fluorescence spectroscopy (XRF) (Spectro Xepos-II) and chemical bonding was

characterized with Fourier Transform Infrared (FTIR) spectroscopy (Thermo Electron Corporation Nicolet Avatar 380).

Figure 1A shows the powder diffraction patterns for the synthesis using the AIC precursor and all reflections can be assigned to γ -Fe₂O₃ (maghemite). The average crystal sizes were refined to 18.8 and 18.6 nm for the uncoated and coated sample, respectively as calculated from the peak broadening.

The crystal sizes are in good agreement with results obtained by in-situ PXRD studies.²⁴ From XRF the Si/Fe molar ratio is 0.1, and pH of the suspension was approximately 6. STEM (Figure 2) shows γ -Fe₂O₃@SiO₂ as a core-shell structure. The diffraction patterns of maghemite (γ -Fe₂O₃) and magnetite (Fe₃O₄) are very similar but the AIC precursor has been shown to produce mainly maghemite.²⁵ From the EDX images in Figure 2 the maghemite particle size is estimated to be approximately 4 nm smaller than the silica shell, and thus the silica layer thickness is ~2 nm (see Figure S20). Additional TEM and HR-TEM are included in Supporting Information Figure S4-S28.

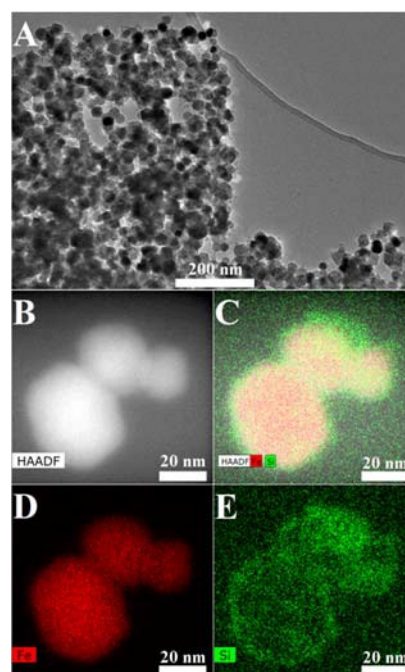


Figure 2: A) TEM image of γ -Fe₂O₃@SiO₂ nanocomposites. B) HAADF view of selected particles. C-E) Elemental maps of Fe (D), Si (E) and a superposition of B, D and E (C). Unreacted TEOS precursor can be seen by a high Si background in C and E.

The crystal size of anatase is also unaffected by the deposition of the secondary material as was the case for γ -Fe₂O₃. Rietveld refinements show that TiO₂ forms phase pure anatase with an average crystallite size of 6.5 nm and 7.3 nm for the coated and uncoated sample, respectively (Figure 1B). This is in agreement with previous results.²¹ The calculated crystal sizes confirm that the silica deposition does not change the observed diffraction pattern except for the addition

of a broad feature at approx. 25° from the amorphous silica. STEM analysis (Figure 3) shows a narrow size distribution, and the HAADF and EDX images show the $\text{TiO}_2@/\text{SiO}_2$ nanocomposite as a core-shell structure with a thin silica shell of approximately 2 nm uniform shell thickness as estimated from comparison of particle sizes in Figure 3D and 3E (see also Figure S28). The concentration of the TEOS precursor was 4 times higher than the TTIP precursor, but from XRF the Si/Ti molar ratio of the collected product is only 1.3. A higher concentration ratio of 4 was selected due to the larger specific surface area of the 7 nm small anatase crystallites.

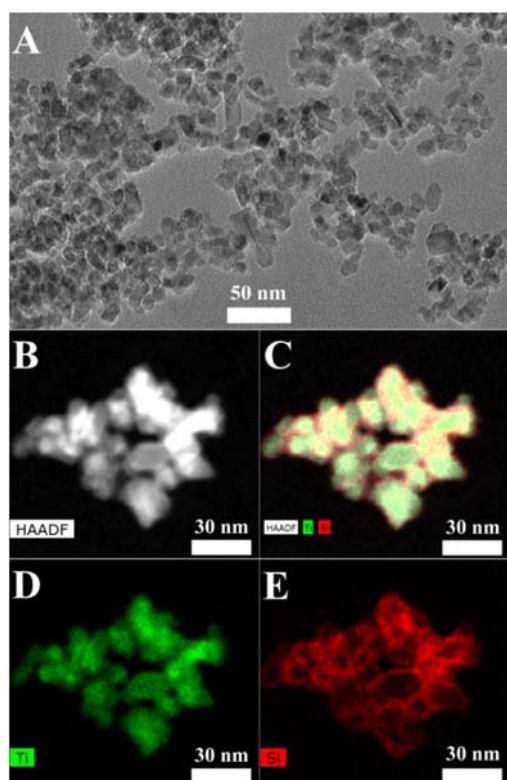


Figure 3: $\text{TiO}_2@/\text{SiO}_2$ core shell nanocomposites A) TEM image of nanocomposites shows particle sizes in good agreement with calculated anatase crystal sizes. B-E) HAADF and EDX images of nanocomposites. A uniform SiO_2 layer up to approximately 2 nm thickness is deposited on TiO_2 .

The two PXRD patterns in Figure 1C show the $\alpha\text{-Fe}_2\text{O}_3$ nanoparticles synthesized at 350°C without and with the deposition of silica. Hematite crystal sizes were $25.0(1)$ nm and $26.0(1)$ nm for the coated and uncoated hematite samples confirming no significant change in core crystal size by the secondary reactor. STEM and EDX images (Figure 4) show the heterogeneous deposition of silica on 20-30 nm hematite nanoparticles. The shell thickness varies from incomplete coverage up to 5 nm thickness. The concentration ratio of the precursors gives an expected Si/Fe ratio of 2, but from XRF the molar ratio of the collected product was 3.5, which shows an iron deficit. This is due to partial dissolution of the hematite nanoparticles as the solvent pH drops to below pH 2 following hydrolysis of the iron

nitrate precursor. The conversion efficiency of TEOS to SiO_2 therefore could not be quantified.

The crystal size of the core nanoparticle is unaffected by the secondary reactor, but can be tuned by changing the synthesis parameters in the first stage of the reactor. To demonstrate this, $\alpha\text{-Fe}_2\text{O}_3$ nanoparticles were first synthesized using only the primary reactor and for temperatures of 250, 300, 350, and 400°C . In all cases all observed diffraction peaks could be assigned to $\alpha\text{-Fe}_2\text{O}_3$ and the refinements of the diffraction peak broadening showed that the crystal size increased with temperature from $19.8(1)$ nm at 250°C to $26.0(1)$ nm at 350°C . (Supporting Information, Figure S2 and S3). These results are in agreement with those obtained by Hao and Teja.²⁶

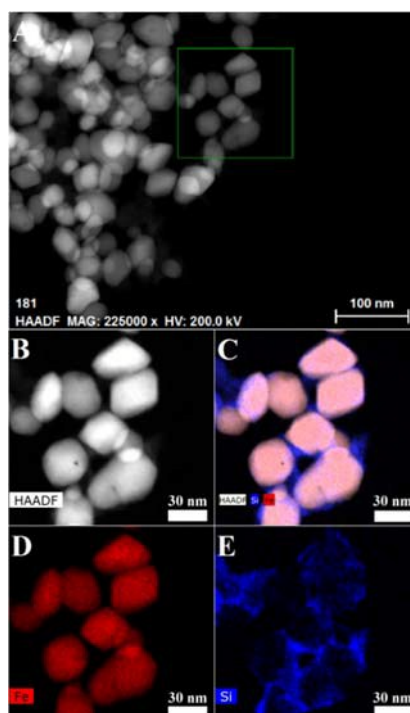


Figure 4: A-B) HAADF images of $\alpha\text{-Fe}_2\text{O}_3@/\text{SiO}_2$ nanocomposites. The hematite core nanoparticles are covered by a non-uniform silica layer of up to 5 nm thickness. C-E) EDX elemental maps of Fe (D) and Si (E) and a superposition of B, D and E (C).

Silica shell formation is highly dependent on the solution pH, while the identity of the metal oxide is likely of lesser importance under the used synthesis conditions. The formation of thin and uniform silica shells on maghemite and anatase indicates that silica formation is unfavourable under the used synthesis conditions and is only formed by heterogeneous deposition. After the formation of a few silica monolayers the particles have the appearance of single silica nanoparticles and further growth is prevented. Highest TEOS to SiO_2 conversion was observed for hematite due to the low pH from the nitrate. For TiO_2 the TEOS conversion decreases to a third due to the higher pH, but the large surface area of the small anatase

nanoparticles increases conversion. For maghemite where pH is close to neutral and the specific surface area is low due to the large crystallite size TEOS conversion is only 5%. The change in silica content can also be observed in the diffraction patterns by the decrease in intensity of the amorphous bump at lower angles. FTIR confirms the presence of SiO₂ for all samples (Supporting Information, Figure S29-S31).

The pH of the solvent for the TiO₂@SiO₂ synthesis used in the primary reactor stage was adjusted to 4 as this is an intermediate of the approximate isoelectric points of silica (pH 2) and anatase (pH 6).²⁷ This results in opposite charges of core and shell material and provides a strong electrostatic driving force for heterogeneous deposition assuming that the isoelectric point of silica nuclei is comparable to that of the bulk value, and that the isoelectric point of anatase is not lowered by adhesion of organic residues. The addition of isopropanol solutions of TTIP and TEOS does not affect the overall pH significantly. Acetic acid is a surfactant and has previously been used for synthesis of silica,^{29,30} but at much higher concentrations than used here, and its role in the current synthesis is therefore limited to pH control. The isoelectric point of maghemite is 6-7 which is close to the pH of the γ -Fe₂O₃@SiO₂ suspension. An increase in temperature, however, may decrease the isoelectric point of oxides.^{31,32}

For α -Fe₂O₃@SiO₂ the solution pH is lower than the isoelectric points of both silica and hematite (pH 8-9).²⁷ Both oxides have positively charged surfaces, and a strong electrostatic attraction is no longer present. Silica formation may be initiated by heterogeneous nucleation, but further silica growth is fast, and the locally available TEOS precursor is rapidly exhausted by the growing silica and not by the core surface. The resulting SiO₂ layer is therefore thick and irregular for the α -Fe₂O₃@SiO₂ sample whereas both maghemite and anatase adopts a uniform core-shell structure when silica is deposited.

In summary, we successfully synthesized γ -Fe₂O₃@SiO₂, TiO₂@SiO₂ and α -Fe₂O₃@SiO₂ nanocomposites of a narrow size distribution. The influence of pH was found to determine the thickness and uniformity of the shell layer by controlling the rate of silica formation. Shell thicknesses of a few nanometers were obtained. The crystal size and structure of the core nanoparticles were unaffected by deposition of silica in the secondary reactor. The results confirm the versatility of the dual-stage flow reactor for the green synthesis of nanocomposites in high yields.

1. F. Cansell and C. Aymonier, *J. Supercrit. Fluids*, 2009, **47**, 508.
2. R. G. Chaudhuri and S. Paria, *Chem. Rev.*, 2012, **112**, 2373.
3. J. Ahn, S. H. Jung, J. H. Lee, K.-Y. Kwon and J. H. Jung, *Bull. Korean Chem. Soc.*, 2013, **34**, 3456.
4. H. S. Lee, S. M. Koo and J. W. Yoo, *J. Ceram. Process. Res.*, 2012, **13**, S300.
5. H. Tong, N. Enomoto, M. Inada, Y. Tanaka and J. Hojo, *Electrochim. Acta*, 2014, **130**, 329.

6. V. Tizjang, M. Montazeri-Pour, M. Rajabi, M. Kari and S. Moghadas, *J. Mater. Sci.: Mater. Electron.*, 2015, **26**, 3008.
7. L. M. Liz-Marzan, M. Giersig and P. Mulvaney, *Langmuir*, 1996, **12**, 4329.
8. J. T. Song, X. S. Zhang, M. Y. Qin and Y. D. Zhao, *Dalton Trans.*, 2015, **44**, 7752.
9. M. W. Zhang, K. G. Fang, M. G. Lin, B. Hou, L. S. Zhong, Y. Zhu, W. Wei and Y. H. Sun, *J. Phys. Chem. C*, 2013, **117**, 21529.
10. X. Zhang, Y. A. Niu, Y. Li and J. P. Zhao, *J. Solid State Chem.*, 2014, **211**, 69.
11. F. Jiang, Y. Fu, Y. Zhu, Z. Tang and P. Sheng, *J. Alloys Compd.*, 2012, **543**, 43.
12. P. S. Mueller, C. P. Parker and S. C. Larsen, *Microporous Mesoporous Mater.*, 2015, **204**, 173.
13. T. N. Narayanan, A. P. R. Mery, P. K. A. Swalih, D. S. Kumar, D. Makarov, M. Albrecht, J. Puthumana, A. Anas and M. R. Anantharaman, *J. Nanosci. Nanotechnol.*, 2011, **11**, 1958.
14. W. Hao, Y. Xi, J. Hu, T. Wang, Y. Du and X. L. Wang, *J. Appl. Phys.*, 2012, **111**, 07B301.
15. H.-J. Zhang, H.-M. Xiong, Q.-G. Ren, Y.-Y. Xia and J.-L. Kong, *J. Mater. Chem.*, 2012, **22**, 13159.
16. X. Tang, E. S. G. Choo, L. Li, J. Ding and J. Xue, *Chem. Mater.*, 2010, **22**, 3383.
17. X. H. Feng, S. K. Zhang and X. Lou, *Colloids Surf. B*, 2013, **107**, 220.
18. W. Stober, A. Fink and E. Bohn, *J. Colloid Interface Sci.*, 1968, **26**, 62.
19. S. H. Liu and M. Y. Han, *Adv. Funct. Mater.*, 2005, **15**, 961.
20. T. Adschiri, K. Kanazawa and K. Arai, *J. Am. Ceram. Soc.*, 1992, **75**, 1019.
21. H. L. Hellstern, J. Becker, J. Hald, M. Bremholm, A. Mamakhel and B. B. Iversen, *Ind. Eng. Chem. Res.*, 2015, **54**, 8500.
22. H. Hayashi and Y. Hakuta, *Mater.*, 2010, **3**, 3794.
23. J. Rodriguez-Carvajal, *Phys. B*, 1993, **192**, 55.
24. H. L. Andersen, K. M. O. Jensen, C. Tyrsted, E. D. Bojesen and M. Christensen, *Cryst. Growth Des.*, 2014, **14**, 1307.
25. K. M. O. Jensen, H. L. Andersen, C. Tyrsted, E. D. Bojesen, A. C. Dippel, N. Lock, S. J. L. Billinge, B. B. Iversen and M. Christensen, *ACS Nano*, 2014, **8**, 10704.
26. Y. L. Hao and A. S. Teja, *J. Mater. Res.*, 2003, **18**, 415.
27. M. Kosmulski, *J. Colloid Interface Sci.*, 2011, **353**, 1.
28. K. Suttiponpanit, J. Jiang, M. Sahu, S. Suvachittanont, T. Charinpanitkul and P. Biswas, *Nanoscale Res. Lett.*, 2011, **6**, 1.
29. L. T. Arenas, C. W. Simm, Y. Gushikem, S. L. R. Dias, C. C. Moro, T. M. H. Costa and E. V. Benvenutti, *J. Braz. Chem. Soc.*, 2007, **18**, 886.
30. B. Karmakar, G. De, D. Kundu and D. Ganguli, *J. Non-Cryst. Solids*, 1991, **135**, 29.
31. V. Rodriguez-Santiago, M. V. Fedkin, D. J. Wesolowski, J. Rosenqvist and S. N. Lvov, *Langmuir*, 2009, **25**, 8101.
32. M. L. Machesky, D. A. Palmer and D. J. Wesolowski, *Geochim. Cosmochim. Acta*, 1994, **58**, 5627.